



## Article

# Surface Solar Radiation Resource Evaluation of Xizang Region Based on Station Observation and High-Resolution Satellite Dataset

Huangjie Kong , Jianguo Wang \*, Li Cai, Jinxin Cao, Mi Zhou and Yadong Fan

School of Electrical Engineering and Automation, Wuhan University, Wuhan 430072, China; khj721@whu.edu.cn (H.K.); cail@whu.edu.cn (L.C.); caojinxin@whu.edu.cn (J.C.); zhoumi927@whu.edu.cn (M.Z.); ydfan@whu.edu.cn (Y.F.)

\* Correspondence: wjg@whu.edu.cn

**Abstract:** Xizang boasts a vast and geographically complex landscape with an average elevation surpassing 4000 m. Understanding the spatiotemporal distribution of surface solar radiation is indispensable for simulating surface processes, studying climate change, and designing photovoltaic power generation and solar heating systems. A multi-dimensional, long-term, spatial, and temporal investigation of solar radiation in Xizang was conducted using three unique datasets, including the difference in surface solar radiation (SSR) between high-resolution satellite and ground station data, the annual and monthly distribution of SSR, and the interannual–monthly–daily variation and the coefficient of hourly variability. Combined with high-resolution elevation data, a strong linear correlation was shown between the radiation and the elevation below 4000 m. Furthermore, analysis reveals greater differences in data between east and west compared to the center, as well as between summer and winter seasons. SSR levels vary in steps, reaching the highest from Ngari to Shigatse and the lowest in a U-shaped area formed by southeastern Shannan and southern Nyingchi. In June, high monthly SSR coverage was the highest of the year. Since 1960, the annual mean SSR has generally exhibited a declining trend, displaying distinctive trends across various seasons and datasets. Owing to intricate meteorological factors, some regions exhibited double peaks in monthly SSR. Finally, we have introduced a solar resource assessment standard, along with a multidimensional evaluation of the resources, and categorized all townships. We offer a thorough analysis of Xizang’s solar radiation to provide a comprehensive understanding, which will help to prioritize recommendations for PV construction in Xizang.

**Keywords:** surface solar radiation; differential analysis; elevation variation; spatiotemporal characteristics; township scale classification



**Citation:** Kong, H.; Wang, J.; Cai, L.; Cao, J.; Zhou, M.; Fan, Y. Surface Solar Radiation Resource Evaluation of Xizang Region Based on Station Observation and High-Resolution Satellite Dataset. *Remote Sens.* **2024**, *16*, 1405. <https://doi.org/10.3390/rs16081405>

Academic Editor:

Joaquín Alonso-Montesinos

Received: 26 February 2024

Revised: 28 March 2024

Accepted: 8 April 2024

Published: 16 April 2024



**Copyright:** © 2024 by the authors. Licensee MDPI, Basel, Switzerland. This article is an open access article distributed under the terms and conditions of the Creative Commons Attribution (CC BY) license (<https://creativecommons.org/licenses/by/4.0/>).

## 1. Introduction

As the global demands for carbon emissions reduction and energy security rise, renewable energy sources, including solar energy, wind energy, hydropower, geothermal energy, etc., are playing an increasingly vital role. Solar radiation also plays a crucial role in controlling the Earth’s atmospheric water and energy cycles, which drive the land surface processes such as plant transpiration and land–atmosphere heat and flux exchange. Additionally, solar radiation is a significant component of the global energy balance and has a profound impact on global climate and biological activities [1]. As an emerging clean energy generation method, applications that rely on solar radiation as the primary energy source have witnessed rapid development [2–4]. Understanding the spatiotemporal distribution of surface solar radiation is indispensable for simulating surface processes, studying climate change, and designing photovoltaic power generation and solar heating systems.

With average elevation surpassing 4000 m, Xizang boasts a vast and geographically complex landscape. It has an abundance of clean energy sources such as solar, wind energy, and hydropower. Due to its high elevation and thin atmosphere, Xizang has the potential to become the key area for the development of solar. As illustrated in Figure 1, the upstream regions of the Jinsha River in Xizang have emerged to be a significant new energy zone, driven by the dual-carbon objectives.

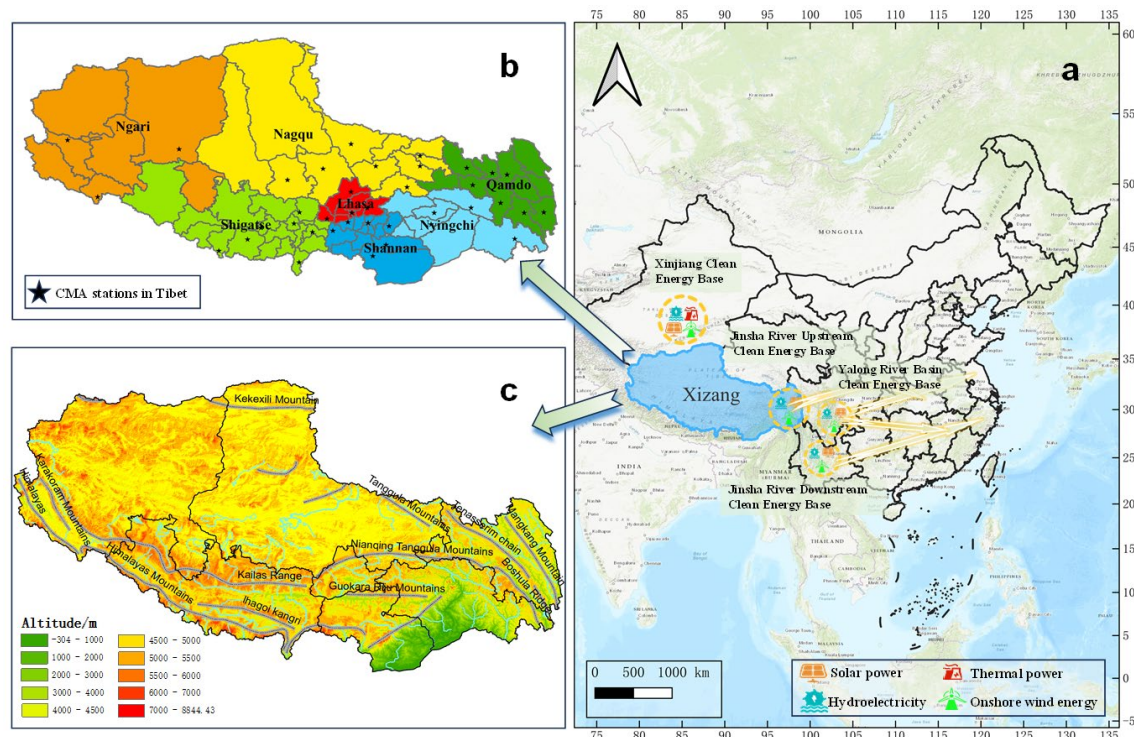


**Figure 1.** The location and topography of study areas: (a) the distribution of study areas in China, including the location of new energy bases, which are planned to deliver energy to other provinces; (b) the distribution of administrative areas in Xizang province and the location of 38 meteorological stations used in this study; (c) the distribution of the topography and major mountain ranges in Xizang province (the elevation map was generated from the ASTER GDEM 30M resolution digital elevation data of the Geospatial Data Cloud).

China's PV construction is growing rapidly and, as of the third quarter of 2023, according to data released by the National Energy Administration of China, had a cumulative grid-connected photovoltaic capacity of 520.4 GW. By 2060, photovoltaic power generation capacity is expected to reach 50 TW. In contrast to Xizang's promise of being one of China's most resource-rich locations for solar energy with annual mean sunshine duration amounting to more than 3000 h [5], the region's PV deployments lag behind the trends [6]. The mismatch between its abundant solar resources and the actual photovoltaic power generation capacity lacked a systematic analysis of solar energy resources in the region. Xizang's solar radiation varies significantly across the region due to factors such as topography and climate. Understanding the spatial and temporal characteristics of solar radiation in Xizang is crucial for policymakers and solar energy project planning, as it can provide valuable guidance for optimal station selection and resource utilization. What is more, such research can help address disparities in energy distribution and consumption among various regions, optimize China's energy structure, and increase the efficiency of natural resource utilization.

Some previous studies used station data to study the temporal and spatial characteristics of solar radiation. For example, Li et al. [7] analyzed the temporal and spatial characteristics of China by using the data of 77 stations; Li et al. [5] analyzed the temporal

and spatial characteristics, interannual variation, and radiation variation coefficient of Xizang. Yang et al. [8] analyzed the long-term trend of solar radiation in China. Tao et al. [9] proposed a method for rasterizing global daily solar radiation and combined the solar radiation model (Bristow–Campbell model) with the meteorological interpolation model (PRISM) to estimate and analyze the spatial distribution pattern of solar radiation daily. Compared with accurate ground-based measurement, the low infrastructure coverage and challenges of equipment maintenance in the Xizang region led to many limitations [10]. According to statistics, there are a total of 756 meteorological stations in China, of which only 122 observe parameters related to solar radiation [11]. Therefore, research based on station data has poor spatial continuity, which hinders the development of the overall radiation environment.

Satellite remote sensing technology offers significant advantages, such as broad coverage and freedom from geographical and time constraints, making it an essential tool in this regard. At present, some scholars have used satellite data to carry out studies on the spatial and temporal characteristics of solar radiation in China. Jin et al. [12] used the fifth-generation European Centre for Medium-Range Weather Forecasts reanalysis (ERA5) data to analyze the spatial distribution and interannual variability of solar radiation across the country, and Yu et al. [13] analyzed the factors affecting solar radiation by using stationary SSR data and satellite meteorological data. Li pointed out that the acquisition of solar radiation data for regional and global assessments can be divided into two periods: before the era of satellite observations and after the advent of satellite-based measurements [14]. Nowadays, satellite and station data can complement each other to a certain extent, helping to provide a deeper understanding of regional solar radiation characteristics. So far, there have been SSR datasets available, such as the Global Energy and Water Exchanges–Surface Radiation Budget (GEWEX-SRB) [15,16], the International Satellite Cloud Climatology Project Flux Data (ISCCP-FD) [17,18], and the Clouds and the Earth’s Radiant Energy System (CERES) [19,20]. However, the satellite products mentioned above either have coarse spatial resolutions or limited time spans, which do not support long-term analyses [21]. The release of long-term ISCCP H-series cloud products has led to the creation of high-precision products [22,23].

So far, there is a lack of research on the spatial and temporal characteristics analysis of Tibet by combining station data and satellite data. Therefore, although Xizang is rich in solar energy, the regional solar energy resource assessment cannot be furthered. A key step in utilizing solar energy is to identify and prioritize the best locations for photovoltaic power plants [24,25], and in order to find suitable solar development sites, the actual solar potential of the ground must first be estimated [26]. Zhang et al. [27] previously estimated China’s solar potential from three aspects: geography, technology, and economy. Yu et al. [28] have conducted a reassessment on a prefecture-level city scale. However, the scope of the above studies is too large to carry out a more detailed analysis on a regional basis. Song et al. [6] pointed out that Xizang should prioritize the construction of large-scale centralized PV power plants, but the Xizang region is vast, and the priority situation of development in each region needs to be studied urgently.

With this objective, this study used ground-based stations and high-resolution global SSR based on ISCCP-H products to carry out data comparison and characterization analysis at multiple scales in time and space; combining high-precision elevation data and focusing on township-level administrative regions, integrated resource assessment indicators were proposed and refined resource classifications were carried out. The research flowchart is shown in Figure 2, and the main contributions of this paper are as follows.

- (1) Analyzed the characteristics of differences between high-resolution product data and station data at spatial and temporal scales in Xizang province.
- (2) Carried out solar radiation variability studies and altitude correlation studies.
- (3) Evaluated Xizang’s solar radiation resources at a multidimensional scale to provide prioritization recommendations for regional development.

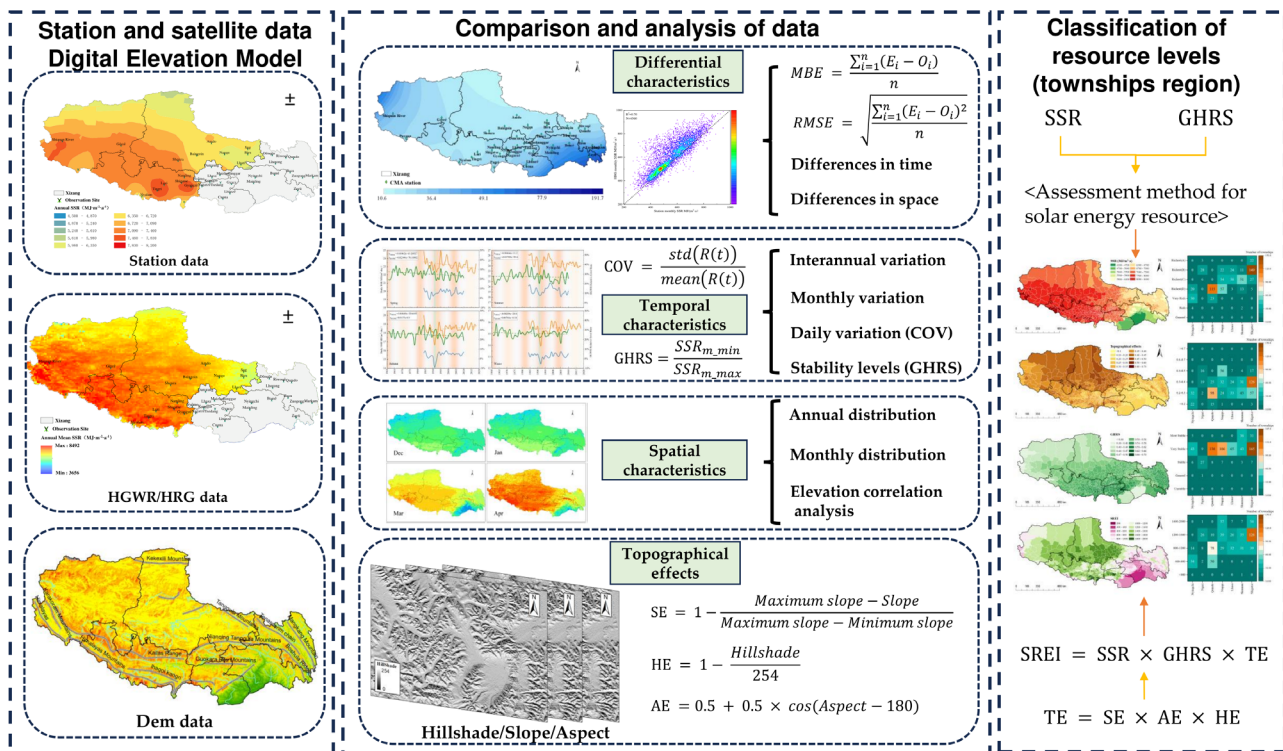


**Figure 2.** The flowchart of solar radiation characteristics and resource evaluation in Xizang.

## 2. Area and Data

### 2.1. Study Area

The Qinghai–Tibetan plateau (QTP), known as the “Roof of the World” and often referred to as the “Third Pole of the World”, encompasses the Xizang region located in its southwestern part. As the study area, Xizang represents the primary area of the plateau and is situated within the geographical coordinates of 78°25′–99°06′E longitude and 26°50′–36°53′N latitude, covering an extensive land area that amounts to over 1.22 million square kilometers, approximately one-eighth of China’s total land area.

Figure 1 also shows the region has 6 prefectural-level cities and 1 district including 8 municipal districts, 64 counties, and 2 county-level cities. With an average elevation of more than 4000 m above sea level, Xizang has 50 peaks above 7000 m. Its complex topography and diverse geomorphologic conditions can be roughly divided into the Himalayan Mountains, the northern Xizang plateau, the southern Xizang valley, and the eastern Xizang alpine valleys. Therefore, despite Xizang’s abundant solar resources, the key challenge lies in how to utilize them efficiently and effectively. In recent years, with population growth and robust economic development, there has been a sharp increase in energy demand, placing significant pressure on both power supply and ecological preservation in Xizang. In vast pastoral areas, the primary sources of energy are livestock dung and firewood. Currently, these methods struggle to meet the energy needs of the daily life and production activities of farmers and herders, and they also have direct or indirect adverse effects on the ecological environment [29].

### 2.2. Data

To evaluate the multi-dimensional spatiotemporal distribution of photovoltaic resources in Xizang, three datasets were employed for the analysis of solar radiation characteristics. These datasets were sourced from the National Tibetan Plateau Data Center (<https://data.tpdc.ac.cn/home/>, accessed on 24 March 2023). The first data were provided by Tang et al. [30] and were derived from the routine meteorological data of the China Meteorological Administration (CMA). They were obtained through the integration of

the Ångström–Prescott model [31] and the artificial neural network (ANN) [32] model for estimation. This exhibited high accuracy in estimating radiation compared to conventional methods. We selected this dataset due to its extended historical coverage and integrity, which greatly facilitates the continuity of our long-term time-series and global analysis. The dataset spans from 1984 to 2010, with a minimum time scale of one day. In this study, we selected data from a total of 38 meteorological stations in Xizang for analysis; the locations and elevation of stations and regions are showed in Figure 1 and Appendix A Table A1.

The second dataset was provided by Feng et al. [21] and was established by integrating three datasets: daily direct radiation data from 121 CMA stations, sunshine duration records from 2400 CMA stations, and ISCCP-HXG cloud products. The estimation process utilized the corrected Ångström–Prescott equation. These datasets were fused through geographically weighted regression (GWR) to generate a high-resolution global surface solar radiation dataset with a 3 h temporal resolution and a spatial resolution of 10 km. HGWR outperforms the Climate Monitoring Satellite Application Facility (CMSAF), ISCCP-HXG, and GEWEX. It has a minimum time scale of one month and spans the months of July 1983 through June 2017.

The third data was provided by Tang et al. [33] and was constructed based on a combination of ISCCP H-series cloud products, the fifth-generation European Centre for Medium-Range Weather Forecasts reanalysis data (ERA5) [34], and Moderate Resolution Imaging Spectroradiometer (MODIS) albedo and aerosol products [35]. The estimation of high-resolution global surface solar radiation (HRG) was achieved using the SUN-FLUX scheme and the aerosol parameterization scheme. It has demonstrated superior performance in terms of accuracy and spatial resolution when compared to global satellite radiation products such as GEWEX-SRB, ISCCP-FD, and CERES. This dataset also offers a temporal resolution of 3 h and a spatial resolution of 10 km. With a one-day minimum time span, it spanned the months of July 1983 through December 2018.

The administrative boundary data are all sourced from DataV.GeoAtlas on the Aliyun data visualization platform. The elevation data of Xizang are derived from the ASTER GDEM 30M resolution digital elevation data of the Geospatial Data Cloud.

### 3. Methods

#### 3.1. Evaluation Metrics and Methods

The accuracy of a data determines its value for use. Since the high-resolution dataset is different from the point distribution of the station, its data points are raster data divided by latitude and longitude. We extracted satellite SSR data (HGWR and HRG) with station data at station locations and choose the repeated time periods (January 2001 to December 2010) for comparison. The approximate spatial distribution of the errors is characterized using the geographic information system interpolation approach. In this paper, mean bias Error (*MBE*) and root mean squared error (*RMSE*) are chosen to evaluate the satellite data.  $R^2$  is the parameter to assess the fitting performance. Most of the published articles use them to evaluate the difference between the data. *MBE* reflects the mean relative error, and *RMSE* to some extent reflects the mean absolute error; thus, their combination is reasonable. Their mathematical expressions are

$$MBE = \frac{\sum_{i=1}^n (E_i - O_i)}{n} \quad (1)$$

$$RMSE = \sqrt{\frac{\sum_{i=1}^n (E_i - O_i)^2}{n}} \quad (2)$$

$$R^2 = 1 - \frac{\sum_{i=1}^n (E_i - O_i)^2}{\sum_{i=1}^n (O_i - \bar{O})^2} \quad (3)$$

where  $E_i$  and  $O_i$  are, respectively, the high-resolution satellite data and station data values ( $\text{MJ}/\text{m}^2$ ), and  $n$  is the amount of data extracted at the station location for comparison

purposes. For smaller error, the *MBE* and *RMSE* should be closer to zero, while the fit is better when  $R^2$  are closing to 1.

### 3.2. Calculation of Variability

To analyze the intraday variability of solar resources in Xizang, we used HRG's 3-hour-by-3-hour SSR data to calculate the coefficient of variation (COV) to measure the hourly variability of SSR.

$$\text{COV} = \frac{\text{std}(R(t))}{\text{mean}(R(t))} \quad (4)$$

COV is the coefficient of variation in period  $t$ ;  $\text{std}(R(t))$  represents the standard deviation of hourly SSR in period  $t$  ( $t$  stands for 8, 11, 14, 17, and 20 o'clock at CST), and  $\text{mean}(R(t))$  represents the average value of hourly SSR in period  $t$ .

### 3.3. Evaluation of Solar Resources

#### 3.3.1. Abundance and Stability Levels of SSR

Práválie suggested that using more categories would be very beneficial for accurately assessing solar energy resources [36]. Therefore, we assess the resource richness and stability level of the solar radiation in the Xizang region based on the "Assessment method for solar energy resource" ((GB/T 37526-2019), <https://webstore.ansi.org/standards/spc/gb375262019>, accessed on 25 February 2024). Meanwhile, since the radiation level in Xizang is much higher than in the rest of China, we have subdivided the original "Richest" category into four levels, A, B, C, and D, to meet the requirements of high SSR in Xizang. The most stable class was also added to the original stability classification. The criteria for ranking resourcefulness are shown in Tables 1 and 2. Annual average SSR was calculated from station data and HGWR data and measured using abundance metrics. Global horizontal radiation stability (GHRS) was used to measure the stability of regional radiation (Equation (5)).

$$\text{GHRS} = \frac{\text{SSR}_{m\_min}}{\text{SSR}_{m\_max}} \quad (5)$$

where  $\text{SSR}_{m\_min}$  and  $\text{SSR}_{m\_max}$  are the minimum and maximum values of average daily total horizontal radiation for the year of calculation, respectively. GHRS is the ratio of them, and steadier yearly radiation is indicated by a higher number.

**Table 1.** The Solar Energy Resource Abundance Levels.

Annual SSR	Resource Level
$\geq 2222 \text{ kW}\cdot\text{h}/(\text{m}^2\cdot\text{a})$ $\geq 8000 \text{ MJ}/(\text{m}^2\cdot\text{a})$	Richest-A
$2083\text{--}2222 \text{ kW}\cdot\text{h}/(\text{m}^2\cdot\text{a})$ $7500\text{--}8000 \text{ MJ}/(\text{m}^2\cdot\text{a})$	Richest-B
$1944\text{--}2083 \text{ kW}\cdot\text{h}/(\text{m}^2\cdot\text{a})$ $7000\text{--}7500 \text{ MJ}/(\text{m}^2\cdot\text{a})$	Richest-C
$1750\text{--}1944 \text{ kW}\cdot\text{h}/(\text{m}^2\cdot\text{a})$ $6300\text{--}7000 \text{ MJ}/(\text{m}^2\cdot\text{a})$	Richest-D
$1400\text{--}1750 \text{ kW}\cdot\text{h}/(\text{m}^2\cdot\text{a})$ $5040\text{--}6300 \text{ MJ}/(\text{m}^2\cdot\text{a})$	Very Rich
$1050\text{--}1400 \text{ kW}\cdot\text{h}/(\text{m}^2\cdot\text{a})$ $3780\text{--}5040 \text{ MJ}/(\text{m}^2\cdot\text{a})$	Rich
$< 1050 \text{ kW}\cdot\text{h}/(\text{m}^2\cdot\text{a})$ $< 3780 \text{ MJ}/(\text{m}^2\cdot\text{a})$	General

**Table 2.** The Global Horizontal Radiation Stability (GHRS) Level.

Grading Threshold	Stability Level
$\text{GHRS} \geq 0.58$	Most Stable
$0.47 \leq \text{GHRS} < 0.58$	Very Stable
$0.36 \leq \text{GHRS} < 0.47$	Stable
$0.28 \leq \text{GHRS} < 0.36$	General
$\text{GHRS} < 0.28$	Unstable

### 3.3.2. Topographic Effect and Solar Resource Evaluation Indicator

The construction of photovoltaic (PV) power generation is constrained by a variety of factors, among which topography significantly affects the exploitability of PV resources. For the construction of photovoltaic power plants, the south-facing slope direction is the most suitable in most areas of China. Simultaneously, a smaller slope ( $0^{\circ}$ – $4^{\circ}$ ) is more appropriate; otherwise, it will result in higher building costs for photovoltaic power plants and an inability to maximize the use of solar energy resources by photovoltaic modules that cannot be adjusted to the ideal inclination angle [37], so the maximum number of degrees of the slope is limited to  $15^{\circ}$ . The three factors of slope effects (SE), aspect effects (AE), and hill-shade effects (HE) in Xizang were calculated by ARCGIS, and the topographic effects (TE) were obtained by using Equations (6)–(9).

$$SE = 1 - \frac{\text{Maximum slope} - \text{Slope}}{\text{Maximum slope} - \text{Minimum slope}} \quad (6)$$

$$AE = 0.5 + 0.5 \times \cos(\text{Aspect} - 180) \quad (7)$$

$$HE = 1 - \frac{\text{Hillshade}}{254} \quad (8)$$

$$TE = SE \times AE \times HE \quad (9)$$

where the *Maximum slope* and *Minimum slope* were selected as  $15^{\circ}$  and  $4^{\circ}$ , respectively. SE is defined as 0 and 1 when the slope is higher than  $15^{\circ}$  and less than  $4^{\circ}$ , respectively. *Slope*, *Aspect*, and *Hillshade* were obtained by ARCGIS using elevation data. All indicators range between 0 and 1, with larger values representing the more suitable ones for building PV plants.

The solar resource assessment indicator (SREI) was introduced to measure the region's priority level for PV resource development, which incorporates SSR values, stability levels, and topographic effects.

$$SREI = SSR \times GHRS \times TE \quad (10)$$

where SSR is the annual average surface solar radiation. The higher the value of SREI, the better the exploitable solar radiation available in the area.

## 4. Results and Analysis

The analysis of solar radiation data in Xizang will be divided into four parts. The first part will focus on comparing the differences between station data and satellite data in Xizang. The second part will analyze the characteristics of SSR distribution. The third part will delve into the characteristics of radiation variations. Lastly, the fourth part will involve the classification of solar resources in Xizang.

### 4.1. Differences between High-Resolution Data and Station Data

Figure 3a,c show the distribution results of difference analysis. The southeast of the Xizang region has larger error numbers for both HGWR and HRG errors. Furthermore, HGWR shows a higher distribution of error values in the western region of Ngari, whereas HRG shows a higher distribution in the northern region of Xizang. Only a few stations in HGWR, namely Basu, Qamdo, Biru, Cuona, Nyalam, and Lazi, showed underestimation, with values of 35.27, 21.97, 18.76, 5.97, 9.95, and 16.32 MJ/(m<sup>2</sup>·month), respectively. The rest of HGWR and all of HRG present obvious overestimation. Many studies have pointed out that satellites will overestimate SSR. Research by Zhang [20] presented that these worldwide products may consistently overstate 80% CMA stations, with the exception of the Tibetan Plateau [38,39]. The negative bias on the Tibetan Plateau, on the other hand, is due to its own highly variable topography and more frequent snowpack, which makes the assessment inaccurate [40,41]. In addition, Zhang [42] and Ma [43] suggested that the primary influencing factors for radiation in western China are aerosols and cloud cover. Yu [13] found aerosols explained 87.0% of the monthly clear-sky SSR over

Qinghai–Tibet Plateau. In the worst-case scenario, absorbing aerosols mix with cloud cover, significantly reducing the top-of-atmosphere (TOA) reflectance, leading to a substantial overestimation of SSR. The interaction between clouds and aerosols may be exacerbated in China due to rapid economic development and high population density, resulting in such overestimations [1,44,45].

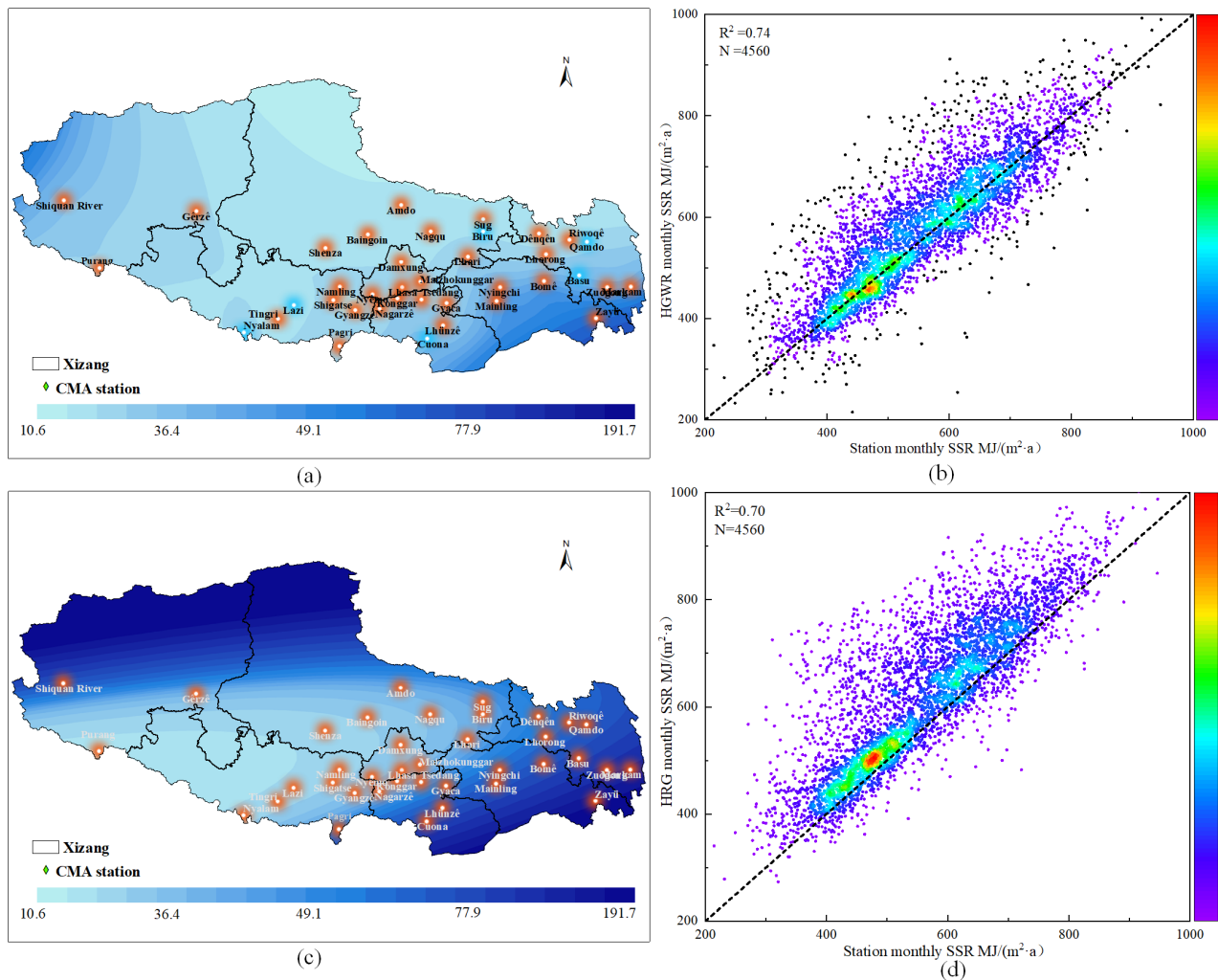


**Figure 3.** Difference maps of monthly SSR (MJ/(m<sup>2</sup>·month)) from (a) HGWR and (c) HRG with stations in 2001–2010. Comparison of monthly SSR from (b) HGWR and (d) HRG with stations in 2001–2010.

Figure 3b,d present the validation results for high-resolution SSR at 38 CMA stations. The  $R^2$  values were 0.74 and 0.70 for HGWR and HRG, respectively. Table 3 lists the performances of high-resolution SSR in different months. The MBE and RMSE were significantly lower in winter than in summer and basically showed a trend of double peaks during the year; while the first peak occurred in May or June, the second occurred in August. This is mostly related to the rainy season, which is covered in more detail in Section 4. The relative error of HRG was even as high as 21.5% in August, compared with 9.7% for HGWR. Therefore, the estimation of HGWR seems to have better performance than HRG in Xizang.

**Table 3.** Comparison of MBE and RMSE between HGWR and HRG with stations in different months.

Month	HGWR_MBE MJ/(m <sup>2</sup> ·Month)	HGWR_RMSE MJ/(m <sup>2</sup> ·Month)	HGWR Relative Error Rate (%)	HRG_MBE MJ/(m <sup>2</sup> ·Month)	HRG_RMSE MJ/(m <sup>2</sup> ·Month)	HRG Relative Error Rate (%)
Jan	3.85	22.9	3.8	21.9	35.2	5.4
Feb	7.5	28.1	4.7	7.2	26.1	4.2
Mar	26.2	39.4	5.7	14.5	44.7	5.3
Apr	28.9	42.9	5.5	47	77.8	7.7
May	30.8	57.1	6.8	86.4	110.9	12.1
Jun	21.5	62.3	6.5	84.5	113.8	12.3
Jul	3.91	51.6	5.9	63.7	95.8	10.3
Aug	38.1	74.2	9.7	118	140.3	21.5
Sep	15.8	43.9	6.4	64.4	85	12.3
Oct	6.2	34.4	4.9	24.8	47.2	6.9
Nov	−0.62	18.2	3.0	17.5	28.4	4.6
Dec	3.31	18.8	3.3	32.1	39.3	7.7

### 4.2. Surface Solar Radiation Distribution in Xizang

#### 4.2.1. Annual and Monthly SSR Distribution

Figures 4 and 5 depict the distribution characteristics of annual and monthly mean SSR in Xizang, respectively. Figure 4a was based on station data and interpolated using the kriging interpolation method of geographic information systems. Figure 4b was based on HGWR data with 10 km resolution. It is evident that there is a high degree of consistency in the distribution based on the two datasets in Figure 4. The overall performance is high in the west and low in the east, with a band of high values located in the Kailas and Himalaya ranges, whose high altitude gives high SSR near the stations of Tingri, Shigatse, and Shiquanhe. The Lhasa region is located between the Kailas, the Guokara Riju, and the Nianqing Tanggula mountain ranges, and the overall SSR is also high; in addition, the high SSR of the Nagqu region is located in the southwest and gradually decreases to the north and east. Influenced by the three major topographies of the Hengduan Mountains, the Nyingchi Tanggula Mountains, and the eastern section of the Himalayas, the SSR of the Shannan and Nyingchi regions are bisected by the Himalayas, with huge differences in SSR. The low values of SSR are located in the U-shaped area surrounded by the stations of Zayü, Bomê, Mainling, Nyingchi, and Cuona. The Qamdo region is relatively low in altitude, and SSR is close to the eastern part of the neighboring Nagqu region.

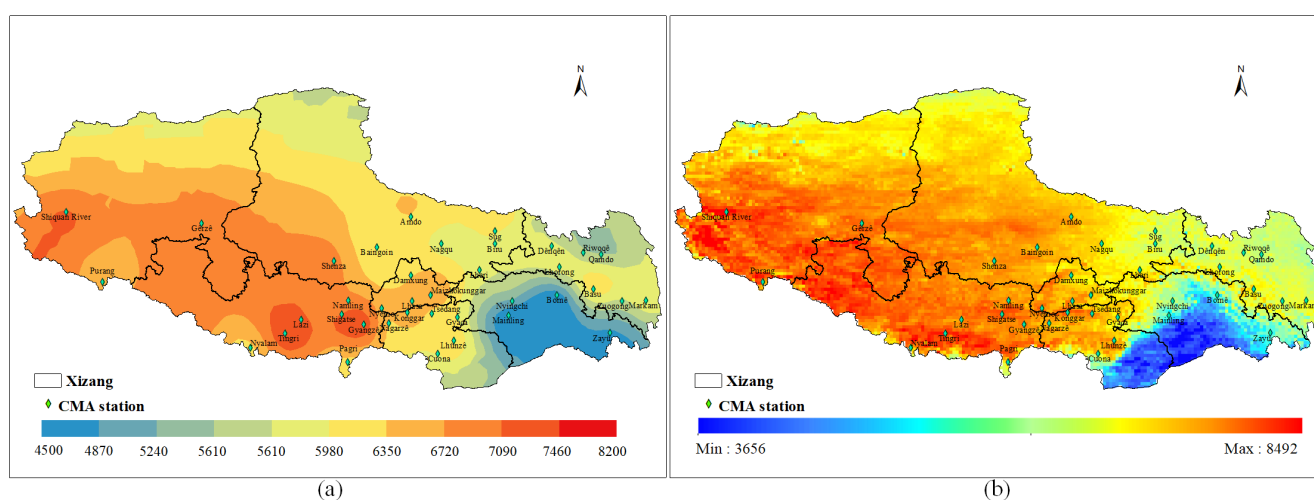


**Figure 4.** Spatial distribution of annual mean SSR (MJ/(m<sup>2</sup>·a)) based on (a) stations and (b) HGWR in 2005–2010.

It can be found in Figure 5 that most areas in Xizang have the lowest SSR in December and January and reach the peak in May and June, with the high values of radiation increas-

ing outward from the area around Ngari to Shigatse and the low values also appearing in the region at the latest. The areas within the U-shaped region, however, show different variations, as indicated by a decrease rather than an increase in February and May, a large drop in September, and an increase rather than a decrease in October. This part will be further understood in conjunction with the monthly variation of SSR in Section 4.3.

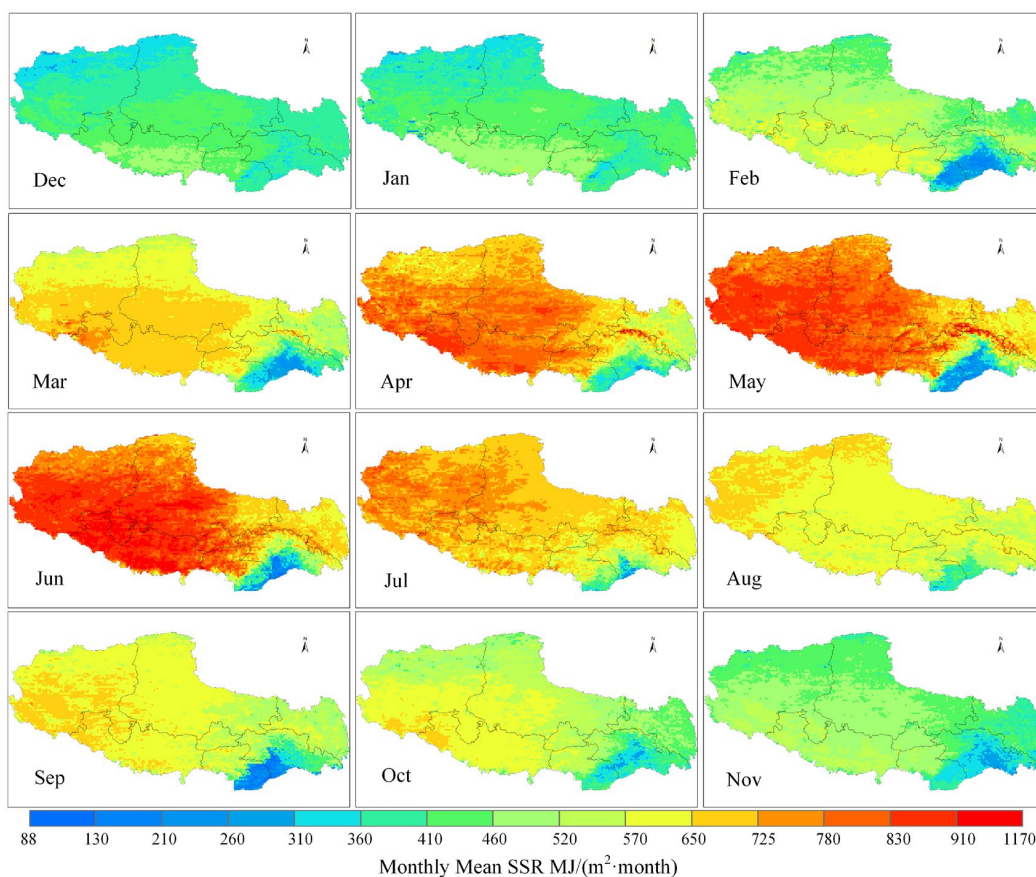


**Figure 5.** Spatial distribution of monthly mean SSR of HGWR in 2015–2017.

#### 4.2.2. Elevation Affecting SSR

SSR in each region is influenced by a number of factors, such as the quality of the local atmosphere, the total amount of ozone columns, and the zenith angle of the sun. However, elevation plays a crucial role in Xizang. As Figure 6 and Table 4 show, Xizang has the largest area at elevations ranging from 4500 to 5000 m. Meanwhile, SSR is quite dispersed around the 3000–3500 m elevation range, covering a wide range from below 4000 to over 8000 MJ/(m<sup>2</sup>·a). But when the elevation exceeds 3000 m, the maximum SSR values remain almost constant, while the minimum SSR values show an increasing trend with elevation.

**Table 4.** SSR (MJ/(m<sup>2</sup>·a)) extremes, means and quartiles at each elevation.

Elevation (m)	Mean SSR	One-QTRs SSR	Three-QTRs	Minimum	Maximum
<2000	4464	4260	4634	3724	5166
2000–3000	4843	4425	5169	3814	6227
3000–3500	6037	5211	6638	3847	8263
3500–4000	6364	5681	6930	4008	8310
4000–4500	6917	6340	7687	4563	8348
4500–5000	7301	6962	7699	5860	8367
5000–5500	7276	6967	7609	6026	8492
5500–6000	7502	7232	7819	6405	8250
>6000	7375	7089	7748	6143	8234

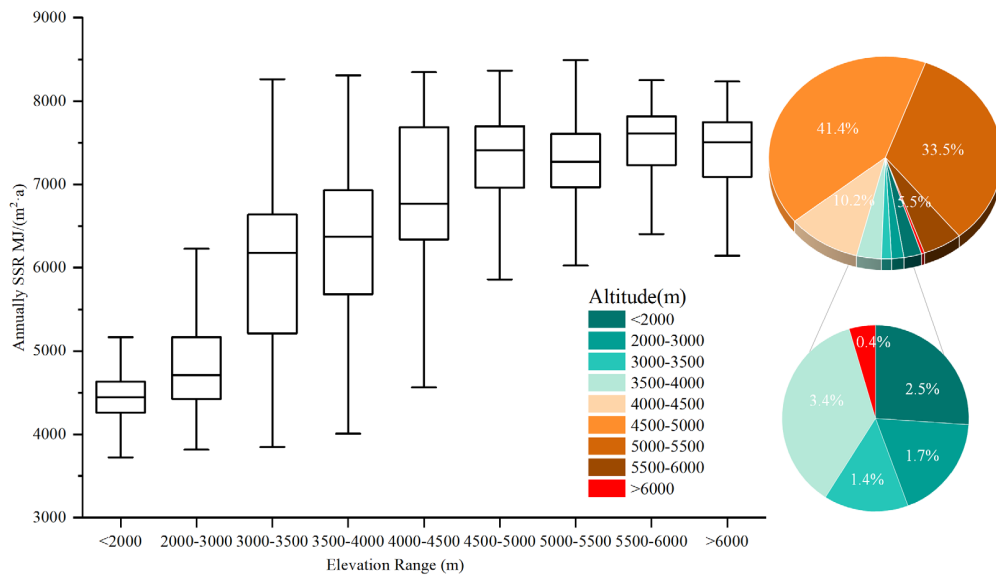


**Figure 6.** Annual mean SSR ( $\text{MJ}/(\text{m}^2 \cdot \text{a})$ ) boxplots and pie chart of area distribution by elevation of Xizang.

We standardized the elevation data and HGWR to the same resolution to analyze the correlation between elevation and annual average SSR. It was revealed that there was a significant positive linear correlation between the two at elevations below 4 km (correlation coefficient of 0.736, significance level (sig) well below 0.01). By fitting the data for SSR and elevation, we derived Equation (11):

$$\text{SSR} = 0.71 \times e + 3465 (e \leq 4000\text{m}) \quad (11)$$

where  $e$  means the elevation of the Xizang region.

Its  $R^2$  value is 0.48, indicating that the model does not adequately capture the variation in SSR. This is understandable since elevation is just one of the factors influencing SSR. In contrast, the region above 4000 m in Xizang is extensive, and the data become more scattered, which makes it challenging to establish a significant correlation between the two. However, the overall trend of the fitted curve aligns with the increase in elevation.

### 4.3. Surface Solar Radiation Variations in Xizang

#### 4.3.1. Interannual Variations

Figure 7 shows the annual mean daily SSR at station locations during 1960–2018. According to Figure 7, Xizang showed a slow increase from 1961 to 1985 and gradually decreased after 1985, returning to a state close to the original radiation level. The daily dose of SSR in Xizang was  $19.235 \text{ MJ}/(\text{m}^2 \cdot \text{day})$  during the period 1961–2011, with a downward trend rate of  $-0.00682 \text{ MJ}/(\text{m}^2 \cdot \text{day})$ . The HGWR daily mean dose of radiation was  $22.4465 \text{ MJ}/(\text{m}^2 \cdot \text{day})$  for the period from 1984 to 2018. The SSR shows an extremely significant decreasing trend from 1984 to 1992. The possible reasons for this phenomenon could include variations in satellite performance, the radiative effects of aerosols from the 1991 Pinatubo volcanic eruption [46], or other unidentified issues in either the satellite or station data. After 1993, SSR returned to  $20 \text{ MJ}/(\text{m}^2 \cdot \text{day})$ . Above that, the linear fitting trend is still decreasing, which is consistent with the results of station data.

December, January, and February are considered to be winter and so on. We analyze the interannual variability of the four seasons as shown in Figure 8, where the two sets of data are more similar at the seasonal scale compared to the annual scale, with satellite data fluctuating more in magnitude. Station data show a decreasing trend in all seasons, with the most pronounced in spring. Sanchez-Lorenzo [47] found the decadal variability in spring over Europe during the period 1983–2010 is the most similar to the annual trends: the same as Xizang. HGWR behaves differently, with a decreasing trend in spring and

summer and an increasing trend in autumn and winter. Based on the historical difference curves between the two datasets, it is evident that the difference between station data and satellite data fluctuates significantly during the spring and summer seasons, while it remains relatively stable during the autumn and winter seasons, with the difference and average relative error not exceeding 2 MJ/(m<sup>2</sup>·day) and 5%, respectively.

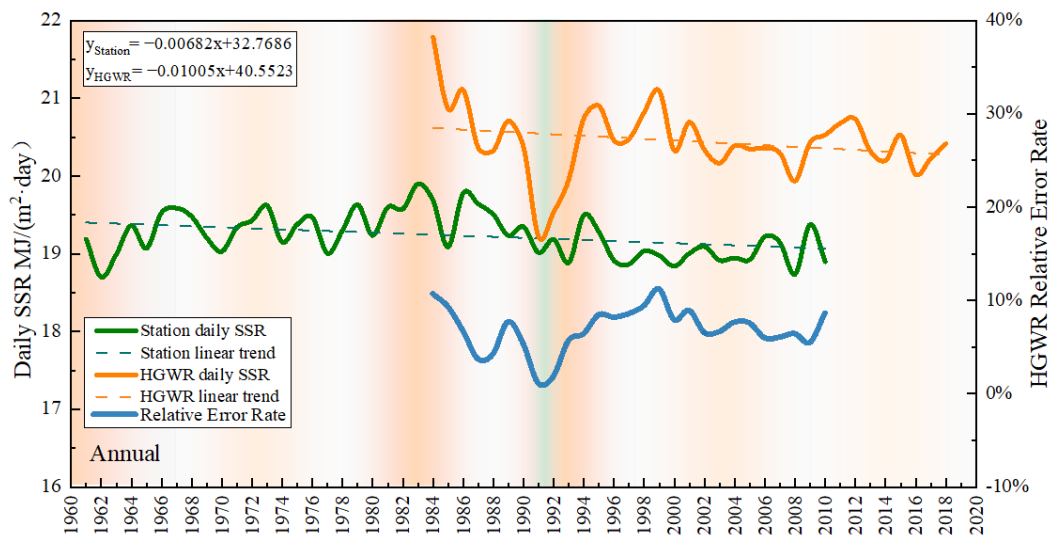


**Figure 7.** The variations of the annual mean daily SSR (MJ/(m<sup>2</sup>·day)) averaged over the Xizang region during 1960–2018 (data of HGWR is extracted at the station locations). The HGWR relative error rate is the proportion of the difference between two datasets in the station data. The orange background shading shows the occurrence and intensity of solar activity, with the green background representing the eruption of Mount Pinatubo.

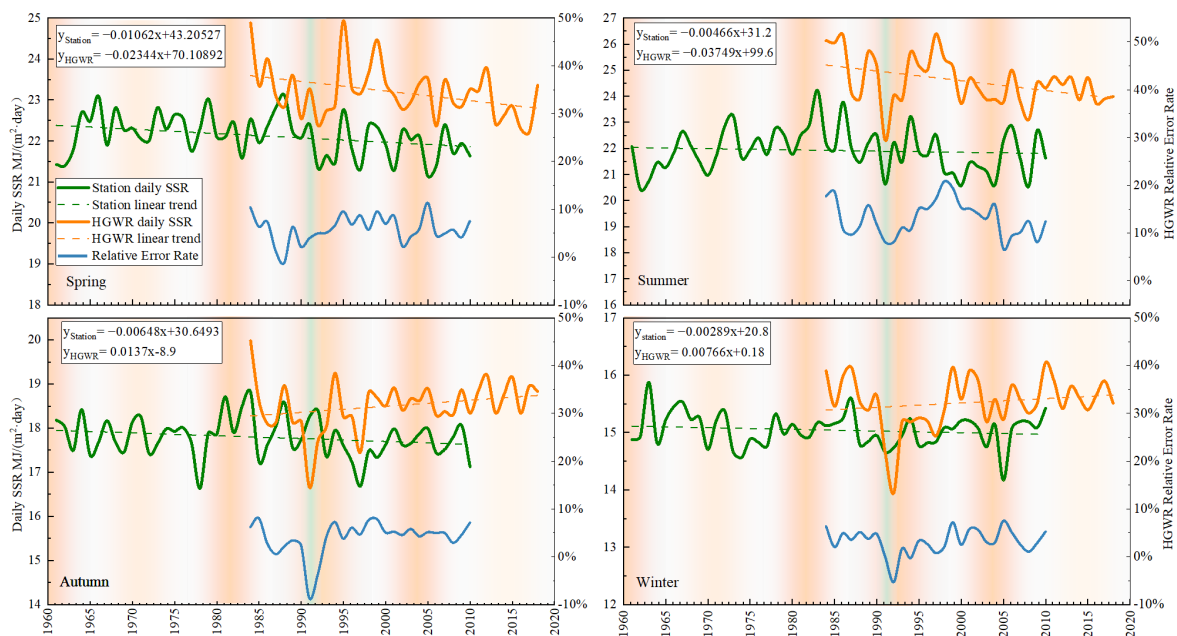


**Figure 8.** The variations of the seasonal mean daily SSR (MJ/(m<sup>2</sup>·day)) averaged over the Xizang region during 1960–2018.

#### 4.3.2. Monthly Variation

Figure 9 shows the station and HGWR monthly mean SSR of each station during 2006 to 2010. Based on station data, the peaks and valleys of SSR generally occurred in June and December, respectively. While some stations peak in May like Nyalam, Lhünzê, and Zuogong

and some in July like Sug, Lhari, Dênqên, Riwoqê, Qamdo, Lhorong, Bomi, Nyingchi, and Mainlin, and even in April like Nagarzê and in March like Pari, the valleys of SSR in Nyingchi City occurred in February and November. From September to October, SSR increased at 17 stations, most of which are located in the eastern region of Xizang. Almost exclusively, the stations in Nagqu and Ngari show a more pronounced single-peak monthly trend. According to Appendix A Figure A1, the annual variation in daily SSR in the eastern, western, and central regions shows that, farther east, the SSR becomes more dispersed. This phenomenon is likely influenced by Xizang's rainy season. Yu [13] pointed out that water vapor has a strong impact on the monthly value of clear-sky SSR. Xizang experiences distinct wet and dry seasons, with the dry season typically occurring from October to the following April. The rainy season spans from May to September. Starting in May, the westerlies predominantly affect convective activities, primarily on the eastern edge. In June, with the strengthening of the Asian summer monsoon and the southwestern monsoon simultaneously, severe convective activities occur in the southeastern region. From July to August, the southwestern monsoon, rising with the topography, brings ample moisture to the eastern and central regions, while convective activities in the western regions are generally weaker [48]. When the rainy season concludes in October, there is a reduction in atmospheric absorption of solar radiation, resulting in increased radiation. In contrast, the western regions, where convective activities are weaker, continue to exhibit a simple unimodal pattern. The monthly trends in HGWR are mostly in line with those in the station data, and winter is the only time of year when monthly SSR levels may fall below those of station data.

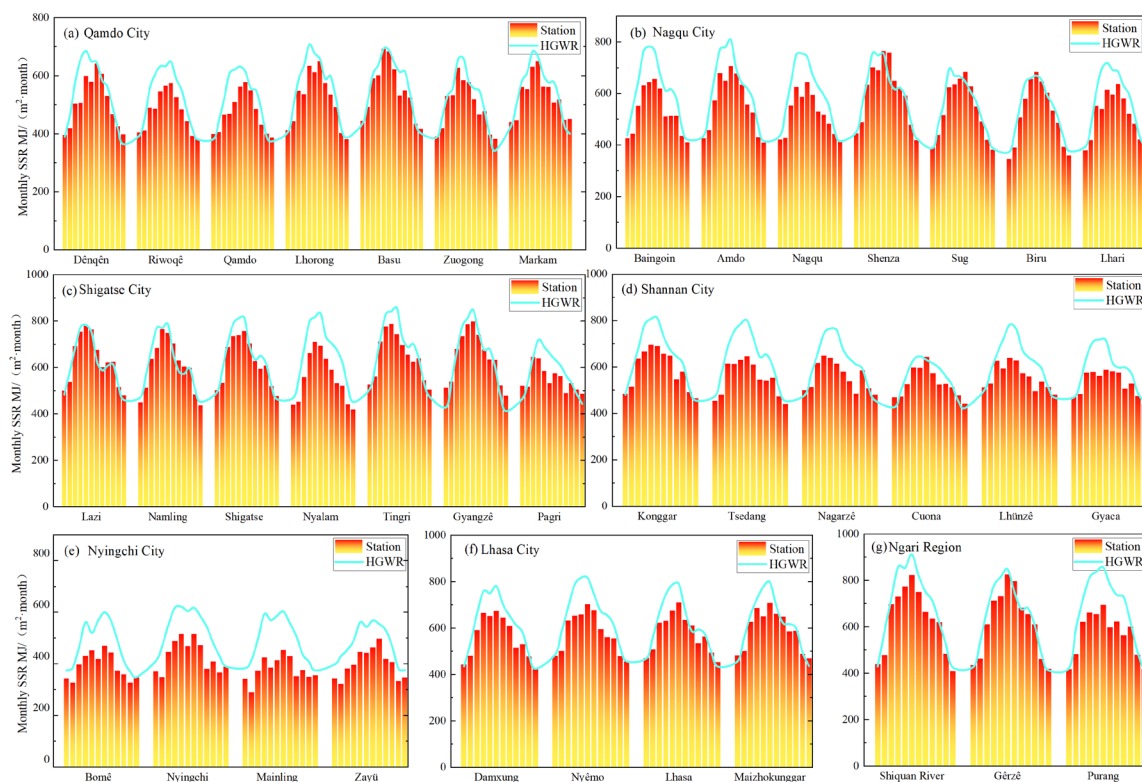


**Figure 9.** Monthly mean SSR ( $\text{MJ}/(\text{m}^2 \cdot \text{month})$ ) from station CMA stations in 2006–2010.

#### 4.3.3. Daily Variation

Figure 10 illustrates the distribution of the coefficient of daily variability. The midday moment in Xizang is within 12:30–13:30. The closest to midday, 14:00, shows the lowest coefficient of variation for the day. At the moment, the Himalayas and its neighboring areas, which are highly radiated, have the lowest coefficient of variation, while other areas also show the best performance compared to other time periods. The coefficient of variation is inevitably high at the moments of 8:00 and 20:00 due to sunrise and sunset. The coefficients

of variation in the whole region at 11:00 and 14:00 basically do not exceed 0.6 and are even lower than 0.3 in the region of Shigatse at 14:00. According to the coefficients of variation during the whole day's sunlight hours, the southeast Xizang region was the highest, followed by parts of the eastern and northern regions. Therefore, the stability of solar radiation is also higher in areas with high radiation in Xizang.

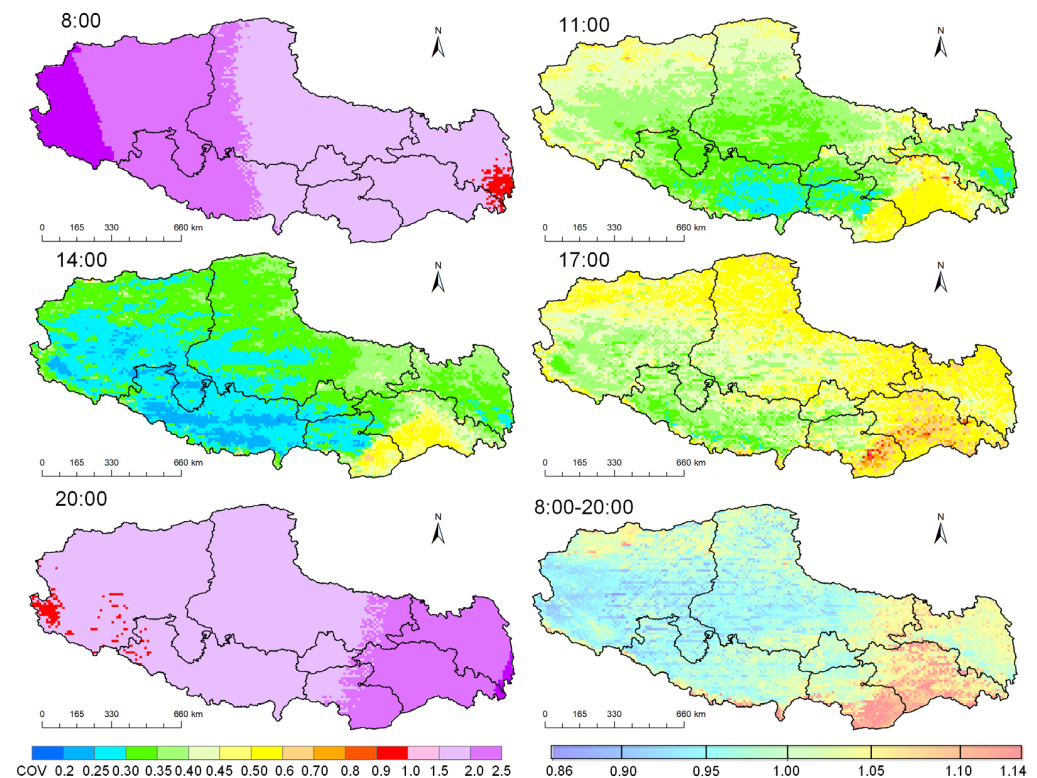


**Figure 10.** Variability of SSR from HRG on an hourly scale in Xizang during 2015 to 2018.

#### 4.4. Analysis of Resource Assessment at the Regional Level in Xizang

Based on the calculated total annual average SSR of the stations, Figure 11 shows the radiation situation in the whole region. Twenty-six stations reached the richest grade, with richest levels (B, C, and D) reaching 3, 7, and 16, respectively. Nine stations are at the very rich level, almost all of them in eastern Xizang. Only three stations in the southeast region are at the rich level.

Figure 12 shows the breakdown of SSR, TE, GHRS, and SREI at the township level. With the exception of Nyingchi, most townships in the area have reached the richest level, with Shigatse having the most numbers of the richest SSR townships. However, topographic conditions are much better in northern Xizang (western Nagqu and eastern Ngari), where most locations have TE values more than 0.4. This is followed by the remainder of Ngari, northwestern Shigatse, and a few areas in Shannan, Qamdo, and southern Shigatse, all reaching values of 0.3 or higher. Areas showing high stability in GHRS are concentrated in south-central Xizang (including eastern Shigatse, southern Nagqu, northern Shannan, southern Nyingchi, and most of Qamdo), with the whole region basically reaching a very stable level. The SREI map shows that areas with high combined developability are mainly located in central Nagqu, followed by southeastern Ngari and northwestern and southern Shigatse. In addition, parts of northeastern Shannan and southeastern Qamdo also have high development priority.

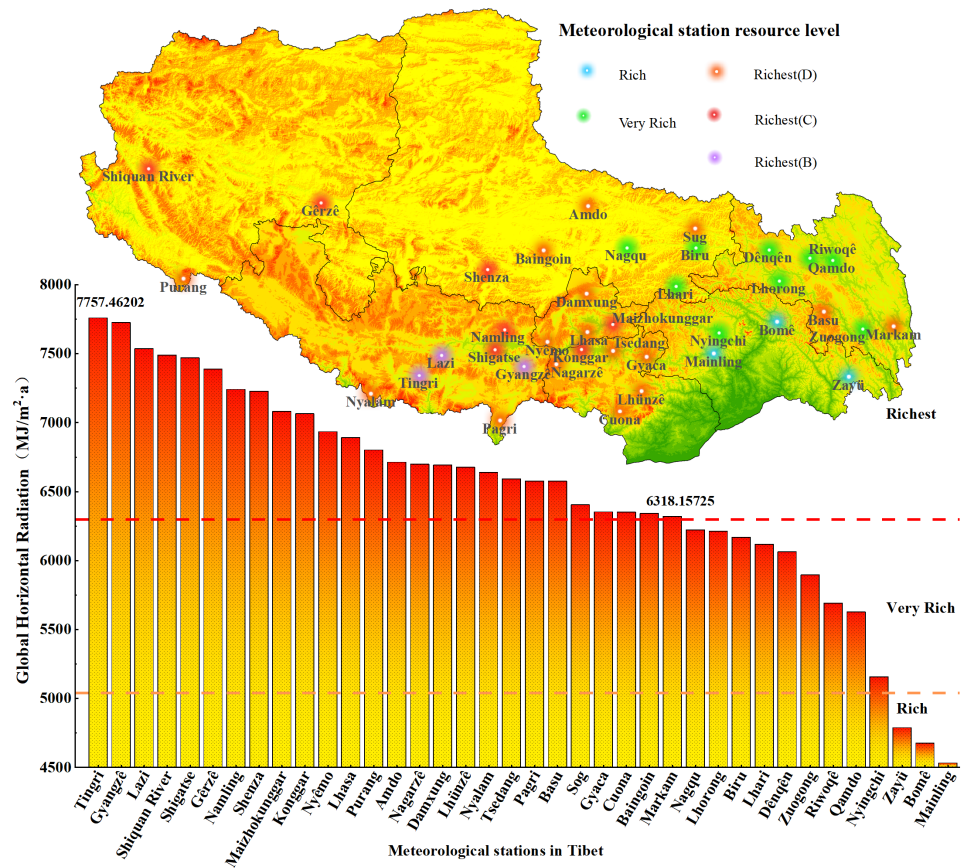


Figure 11. Annual average SSR from station data in 2006–2010 and classification of resources (the red, orange, and blue points represent the richest, very rich, and rich, respectively).

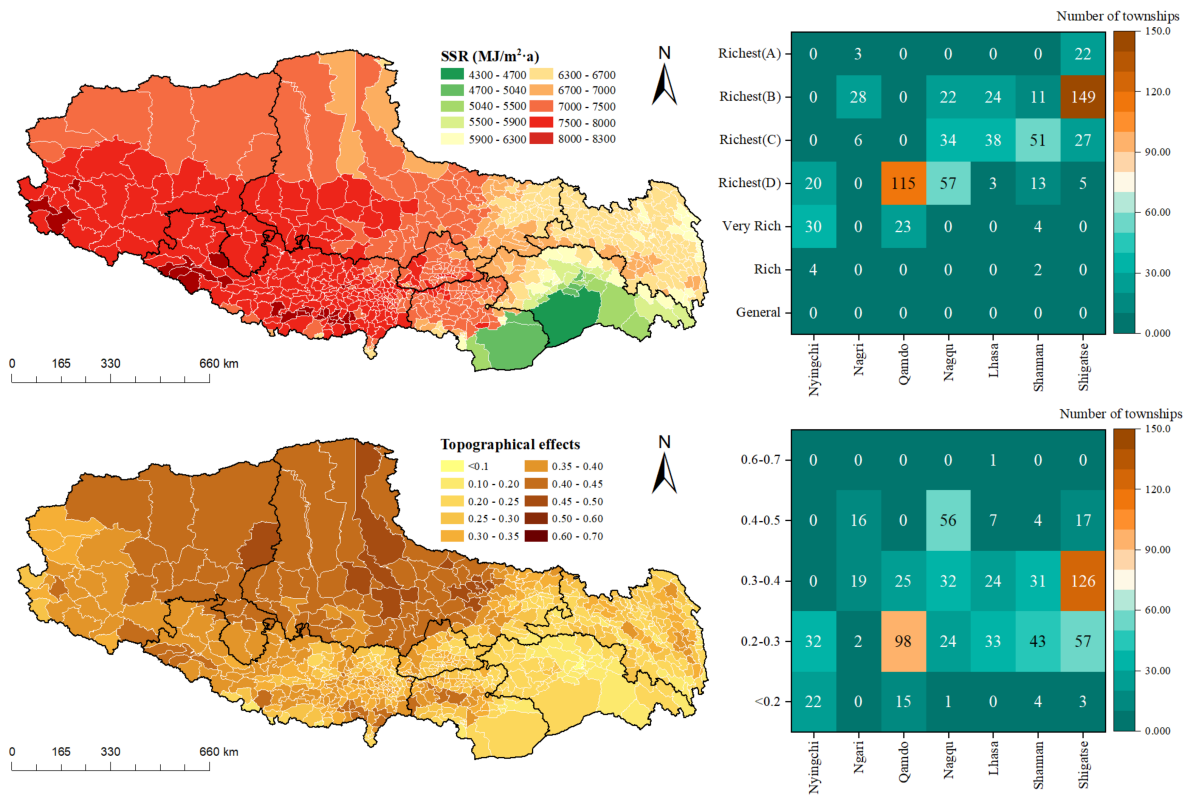
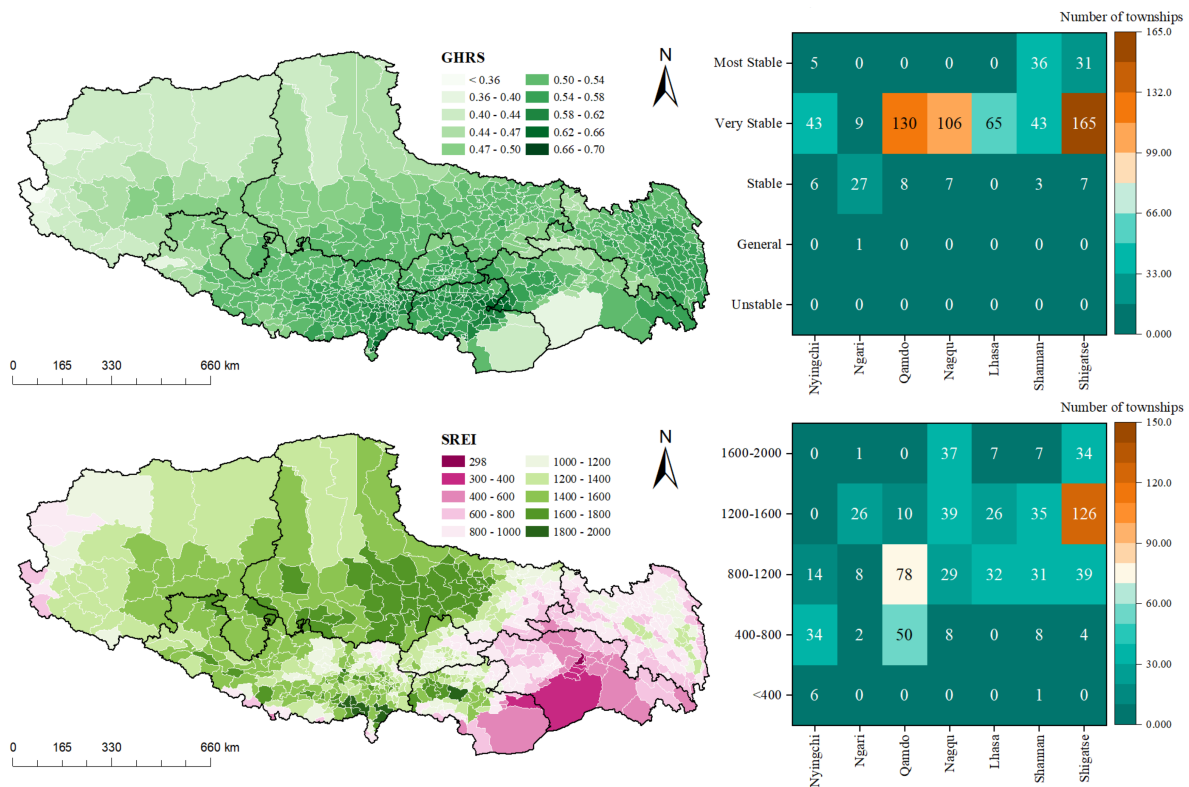


Figure 12. Cont.



**Figure 12.** Distribution map of the surface solar radiation (SSR), topographical effects (TE), global horizontal radiation stability (GHRS), and solar resource assessment indicator (SREI) classification on township scale (left). Heat map of the number of townships at classification in seven regions (right).

## 5. Discussion

Li et al. [49] compared six satellite datasets with 16 stations and found that the eastern part of the Tibetan Plateau had better validation results than the southern part, whereas there was no clear conclusion due to the limited number of validation stations in the western part. The high-resolution dataset used in our study compared more stations and found that the data performed better in the southern region than in the eastern and western regions. This may be due to the fact that the dataset used itself incorporates station data, so the accuracy may be higher in areas with a higher number of stations, but it cannot be ruled out that the eastern region shows higher errors due to climate and other factors. In addition, the above and other studies also found that the validation accuracy was lower in the spring and summer seasons relative to the autumn and winter seasons. This is consistent with the conclusion of this paper that the differences mainly peak in May and August [1].

In terms of spatial scale, Ren et al. [50] found a bias correlation coefficient  $R$  of 0.471 and a coefficient of variation (COV) of 0.0173 between elevation and solar radiation in the Xizang region using station measurements, while we found an  $R$ -squared of 0.48 and a COV of 0.71 below 4 km using high-precision datasets and elevation data.

Jin et al. [12] analyzed the decadal trend of ERA5 and pointed out that the Tibetan Plateau showed a negative trend throughout the year, spring and summer. This is consistent with our findings, but in the fall and winter, the high-resolution data show an increasing trend, which is the opposite of the station data. The station data showed an overall negative trend in both the whole year and in seasons. The monthly variation of SSR in different regions of Xizang is influenced by the local geography and environment. In the western part of Xizang, it typically shows a simple single-peak pattern, whereas in the eastern regions, the timing of the lowest month of SSR showed bimodal or variable characteristics. Furthermore, previous studies have found that SSR variability in most areas of Xizang is less than 26% in spring and summer and greater than 30% in autumn and winter [51]. This paper focuses on the analysis of regional variability in the different periods of a day,

expanding the study of variability in Xizang. The variability was found to be high in the west and low in the east, with the U-shaped region being the highest in the whole region and the lowest in the whole region at 14:00 local time.

For resource evaluation, Yu's research shows that the area with the highest technical potential for large-scale photovoltaic power plants nationwide is Nagqu, Xizang (about 7.3 TW) [28]. The SREI indicators in this paper also reflect the fact that Nagqu has a higher priority for development in Xizang than other regions. If the above area can be better developed, it will provide great support for new energy security and utilization.

## 6. Conclusions

By combining station data with high-resolution global SSR based on ISCCP-H products, this paper analyzes various aspects of solar radiation in Xizang. Differences between high-resolution data and station data and the spatial and temporal characteristics of Xizang at the annual and monthly scales were analyzed, including variability at the daily scale and an elevation correlation study. Finally, solar radiation was assessed and classified at the township scale in conjunction with resource assessment methods.

Overall, the high-resolution data show an overestimation in Xizang, and the data variability is higher on the east and west sides of Xizang and reaches the maximum overestimation in May and August; the radiation in Xizang is high in the west and low in the east, with the high values mainly concentrated in southern Xizang and the low values within the U-shaped region in southeastern Xizang, and there is a large discrepancy between the monthly variations of the solar radiation in this region and those in the rest of the country. Below 4 km, radiation and altitude show a significant positive correlation. The coefficient of daily variability is low in most areas of Ngari Nagqu and Shigatse. Combining SSR, GHRS, and TE, the SREI is obtained to indicate that regions such as Nagqu in Xizang have a high priority in developing large-scale PV power plants.

Overall, Xizang has a special geographical location, and carrying out more in-depth spatial and temporal characterization requires the support of data with higher spatial and temporal resolution, and more influencing factors can be incorporated in the future in planning and developing PV construction.

**Author Contributions:** Conceptualization, J.W. and H.K.; methodology, H.K.; software, H.K.; validation, H.K.; formal analysis, H.K.; investigation, H.K.; resources, H.K.; data curation, H.K.; writing—original draft preparation, H.K.; writing—review and editing, J.W., L.C. and H.K.; visualization, H.K.; supervision, J.C., M.Z. and Y.F.; project administration, J.W.; funding acquisition, L.C. All authors have read and agreed to the published version of the manuscript.

**Funding:** This research was funded by the National Natural Science Foundation of China under Grants 52177154 and the Fundamental Research Funds for the Central Universities under Grants 2042023kf0183.

**Data Availability Statement:** Station data in this paper can be accessed from Repository: Tang, W. (2019). Daily average solar radiation dataset of 716 weather stations in China (1961–2010). National Tibetan Plateau/Third Pole Environment Data Center. <https://doi.org/10.11888/AtmosphericPhysics.tpe.249399.file>. <https://cstr.cn/18406.11.AtmosphericPhysics.tpe.249399.file>. HGWR in this paper can be accessed from Repository: Feng, F., Wang, K. High spatial resolution (10 km) surface solar radiation dataset with by merging sunshine hours over China (1983–2017). National Tibetan Plateau/Third Pole Environment Data Center. <https://doi.org/10.11888/Meteoro.tpcdc.271023>. <https://cstr.cn/18406.11.Meteoro.tpcdc.271023>. HRG in this paper can be accessed from Repository: Tang, W. (2019). Dataset of high-resolution (3 h, 10 k global surface solar radiation (1983–2018). National Tibetan Plateau/Third Pole Environment Data Center. <https://doi.org/10.11888/Meteoro.tpcdc.270112>. <https://cstr.cn/18406.11.Meteoro.tpcdc.270112>.

**Acknowledgments:** The datasets are provided by the National Tibetan Plateau/Third Pole Environment Data Center (<http://data.tpcdc.ac.cn>). We would like to thank Fei Feng, Kaicun Wang and Wenjun Tang et al. for their outstanding contributions and the institutions that provided source data for the above datasets.

**Conflicts of Interest:** The authors declare no conflicts of interest.

## Appendix A

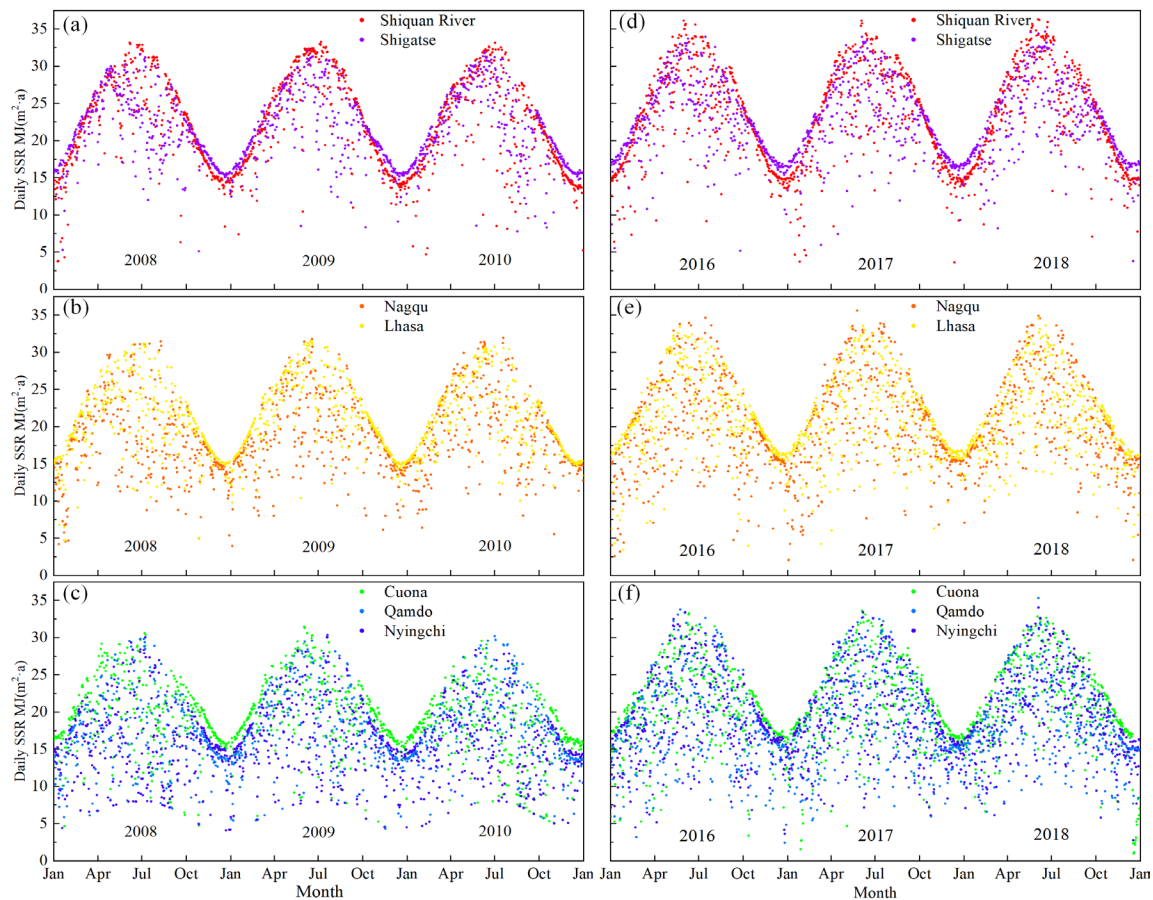


**Figure A1.** The annual variation of daily SSR ( $\text{MJ}/(\text{m}^2 \cdot \text{day})$ ) in Xizang, including (a–c) from stations and (d–f) from HRG (Shiquan River and Shigatse represent the western region, Nagqu and Lhasa represent the central region, and Cuona, Qamdo, and Nyingchi represent the eastern region).

**Table A1.** Elevation information for each region and the location and elevation of the stations mentioned.

Region	Region Elevation Range (m)	Average Elevation/Elevation Standard Deviation (m)	Station	Coordinates	Elevation (m)
Ngari	2596 to 7688	4460/520	Gêrzê	[84.416667, 32.15]	4416.1
			Purang	[81.25, 30.283333]	3901.2
			Shiquan River	[80.083333, 32.5]	4279.8
Qamdo	2016 to 6800	3627/1328	Markam	[98.6, 29.683333]	3871.2
			Zuogong	[97.833333, 29.666667]	3781.2
			Qamdo	[97.166667, 31.15]	3316.2
			Basu	[96.916667, 30.05]	3261
			Riwoqê	[96.6, 31.216667]	3811.2
			Lhorong	[95.833333, 30.75]	3641.2
Lhasa	3437 to 7124	4824/508	Dênqên	[95.6, 31.416667]	3874.3
			Maizhokunggar	[91.733333, 29.85]	3805.1
			Damxung	[91.1, 30.483333]	4201.2
			Lhasa	[91.133333, 29.666667]	3650.1
			Nyêmo	[90.166667, 29.433333]	3810.6

Table A1. Cont.

Region	Region Elevation Range (m)	Average Elevation/Elevation Standard Deviation (m)	Station	Coordinates	Elevation (m)
Nyingchi	−304 to 7427	3627/1328	Zayü	[97.466667, 28.65]	2328.8
			Bomê	[95.766667, 29.866667]	2737.2
			Nyingchi	[94.333333, 29.666667]	2993
			Mainling	[94.216667, 29.216667]	2951.2
Nagqu	3038 to 6934	3662/1603	Sug	[93.783333, 31.883333]	4024
			Biru	[93.783333, 31.483333]	3941.2
			Lhari	[93.283333, 30.666667]	4490
			Nagqu	[92.066667, 31.483333]	4508.2
			Amdo	[91.1, 32.35]	4801.2
			Baingoin	[90.016667, 31.383333]	4701.2
Shigatse	662 to 8824	4980/480	Shenza	[88.633333, 30.95]	4673.2
			Gyangzê	[89.6, 28.916667]	4041.2
			Namling	[89.1, 29.683333]	4001.3
			Pagri	[89.083333, 27.733333]	4301.2
			Shigatse	[88.883333, 29.25]	3837.2
			Lazi	[87.6, 29.083333]	4001.2
			Tingri	[87.083333, 28.633333]	4301.2
Shannan	5 to 7499	3662/1603	Nyalam	[85.966667, 28.183333]	3811.2
			Gyaca	[92.583333, 29.15]	3261.2
			Lhünzê	[92.466667, 28.416667]	3861
			Cuona	[91.95, 27.983333]	4281.3
			Tsedang	[91.766667, 29.266667]	3561.5
			Konggar	[90.983333, 29.3]	3556.5
			Nagarzê	[90.4, 28.966667]	4433.7

## References

- Zhang, X.; Liang, S.; Wang, G.; Yao, Y.; Jiang, B.; Cheng, J. Evaluation of the reanalysis surface incident shortwave radiation products from NCEP, ECMWF, GSFC, and JMA using satellite and surface observations. *Remote Sens.* **2016**, *8*, 225. [\[CrossRef\]](#)
- Besharat, F.; Dehghan, A.A.; Faghieh, A.R. Empirical models for estimating global solar radiation: A review and case study. *Renew. Sustain. Energy Rev.* **2013**, *21*, 798–821. [\[CrossRef\]](#)
- Duzen, H.; Aydin, H. Sunshine-based estimation of global solar radiation on horizontal surface at Lake Van region (Turkey). *Energy Convers. Manag.* **2012**, *58*, 35–46. [\[CrossRef\]](#)
- Teke, A.; Yildirim, H.B.; Celik, O. Evaluation and performance comparison of different models for the estimation of solar radiation. *Renew. Sustain. Energy Rev.* **2015**, *50*, 1097–1107. [\[CrossRef\]](#)
- Li, R.; Zhao, L.; Wu, T.; Ding, Y.; Xin, Y.; Zou, D.; Xiao, Y.; Jiao, Y.; Qin, Y.; Sun, L. Temporal and spatial variations of global solar radiation over the Qinghai–Tibetan Plateau during the past 40 years. *Theor. Appl. Climatol.* **2013**, *113*, 573–583. [\[CrossRef\]](#)
- Song, Z.; Cao, S.; Yang, H. Assessment of solar radiation resource and photovoltaic power potential across China based on optimized interpretable machine learning model and GIS-based approaches. *Appl. Energy* **2023**, *339*, 121005. [\[CrossRef\]](#)
- Li, P.; Gao, X.; Jiang, J.; Yang, L.; Li, Y. Spatial and temporal patterns of solar radiation in China from 1957 to 2016. *Sci. Cold Arid Reg.* **2022**, *14*, 68–78.
- Yang, X.; Qin, W.; Wang, L.; Zhang, M.; Niu, Z. Long-term variations of surface solar radiation in China from routine meteorological observations. *Atmos. Res.* **2021**, *260*, 105715. [\[CrossRef\]](#)
- Pan, T.; Wu, S.; Dai, E.; Liu, Y. Estimating the daily global solar radiation spatial distribution from diurnal temperature ranges over the Tibetan Plateau in China. *Appl. Energy* **2013**, *107*, 384–393. [\[CrossRef\]](#)
- Tang, P.; Xu, B.; Tian, D.; Ren, J.; Li, Z. Temporal and spatial variations of meteorological elements and reference crop evapotranspiration in Alpine regions of Tibet, China. *Environ. Sci. Pollut. Res.* **2021**, *28*, 36076–36091. [\[CrossRef\]](#)
- Zhang, J.; Zhao, L.; Deng, S.; Xu, W.; Zhang, Y. A critical review of the models used to estimate solar radiation. *Renew. Sustain. Energy Rev.* **2017**, *70*, 314–329. [\[CrossRef\]](#)
- Jin, H.; Wang, S.; Yan, P.; Qiao, L.; Sun, L.; Zhang, L. Spatial and temporal characteristics of surface solar radiation in China and its influencing factors. *Front. Environ. Sci.* **2022**, *10*, 916748. [\[CrossRef\]](#)
- Yu, L.; Zhang, M.; Wang, L.; Qin, W.; Jiang, D.; Li, J. Variability of surface solar radiation under clear skies over Qinghai-Tibet Plateau: Role of aerosols and water vapor. *Atmos. Environ.* **2022**, *287*, 119286. [\[CrossRef\]](#)

14. Li, Z.; Moreau, L.; Arking, A. On solar energy disposition: A perspective from observation and modeling. *Bull. Am. Meteorol. Soc.* **1997**, *78*, 53–70. [[CrossRef](#)]
15. Gui, S.; Liang, S.; Li, L. Evaluation of satellite-estimated surface longwave radiation using ground-based observations. *J. Geophys. Res.* **2010**, *115*, D18. [[CrossRef](#)]
16. Zhang, T.; Stackhouse, P.W., Jr.; Gupta, S.K.; Cox, S.J.; Mikovitz, J.C. The validation of the GEWEX SRB surface longwave flux data products using BSRN measurements. *J. Quant. Spectrosc. Radiat. Transf.* **2015**, *150*, 134–147. [[CrossRef](#)]
17. Alexandri, G.; Georgoulas, A.K.; Meleti, C.; Balis, D.; Kourtidis, K.A.; Sanchez-Lorenzo, A.; Trentmann, J.; Zanis, P. A high resolution satellite view of surface solar radiation over the climatically sensitive region of Eastern Mediterranean. *Atmos. Res.* **2017**, *188*, 107–121. [[CrossRef](#)]
18. Qin, J.; Yang, K.; Liang, S.; Zhang, H.; Ma, Y.; Guo, X.; Chen, Z. Evaluation of surface albedo from GEWEX-SRB and ISCCP-FD data against validated MODIS product over the Tibetan Plateau. *J. Geophys. Res. Atmos.* **2011**, *116*, D24. [[CrossRef](#)]
19. Smith, G.L.; Priestley, K.J.; Loeb, N.G.; Wielicki, B.A.; Charlock, T.P.; Minnis, P.; Doelling, D.R.; Rutan, D.A. Clouds and Earth Radiant Energy System (CERES), a review: Past, present and future. *Adv. Space Res.* **2011**, *48*, 254–263. [[CrossRef](#)]
20. Zhang, X.; Liang, S.; Wild, M.; Jiang, B. Analysis of surface incident shortwave radiation from four satellite products. *Remote Sens. Environ.* **2015**, *165*, 186–202. [[CrossRef](#)]
21. Feng, F.; Wang, K. Merging high-resolution satellite surface radiation data with meteorological sunshine duration observations over China from 1983 to 2017. *Remote Sens.* **2021**, *13*, 602. [[CrossRef](#)]
22. Rossow, W.B.; Knapp, K.R.; Young, A.H. International satellite cloud climatology project: Extending the record. *J. Clim.* **2022**, *35*, 141–158.
23. Young, A.H.; Knapp, K.R.; Inamdar, A.; Hankins, W.; Rossow, W.B. The international satellite cloud climatology project H-Series climate data record product. *Earth Syst. Sci. Data* **2018**, *10*, 583–593. [[CrossRef](#)]
24. Vafaiepour, M.; Zolfani, S.H.; Varzandeh, M.H.M.; Derakhti, A.; Eshkalag, M.K. Assessment of regions priority for implementation of solar projects in Iran: New application of a hybrid multi-criteria decision making approach. *Energy Convers. Manag.* **2014**, *86*, 653–663. [[CrossRef](#)]
25. Gunderson, I.; Goyette, S.; Gago-Silva, A.; Quiquerez, L.; Lehmann, A. Climate and land-use change impacts on potential solar photovoltaic power generation in the Black Sea region. *Environ. Sci. Policy* **2015**, *46*, 70–81. [[CrossRef](#)]
26. Mahtta, R.; Joshi, P.K.; Jindal, A.K. Solar power potential mapping in India using remote sensing inputs and environmental parameters. *Renew. Energy* **2014**, *71*, 255–262. [[CrossRef](#)]
27. Zhang, Y.; Ren, J.; Pu, Y.; Wang, P. Solar energy potential assessment: A framework to integrate geographic, technological, and economic indices for a potential analysis. *Renew. Energy* **2020**, *149*, 577–586. [[CrossRef](#)]
28. Yu, S.; Han, R.; Zhang, J. Reassessment of the potential for centralized and distributed photovoltaic power generation in China: On a prefecture-level city scale. *Energy* **2023**, *262*, 125436. [[CrossRef](#)]
29. Jia, A.; Jiang, B.; Liang, S.; Zhang, X.; Ma, H. Validation and spatiotemporal analysis of CERES surface net radiation product. *Remote Sens.* **2016**, *8*, 90. [[CrossRef](#)]
30. Tang, W.; Yang, K.; Qin, J.; Min, M. Development of a 50-year daily surface solar radiation dataset over China. *Sci. China Earth Sci.* **2013**, *56*, 1555–1565. [[CrossRef](#)]
31. Angstrom, A. Solar and terrestrial radiation. Report to the international commission for solar research on actinometric investigations of solar and atmospheric radiation. *Q. J. R. Meteorol. Soc.* **1924**, *50*, 121–126. [[CrossRef](#)]
32. Tang, W.-J.; Yang, K.; Qin, J.; Cheng, C.; He, J. Solar radiation trend across China in recent decades: A revisit with quality-controlled data. *Atmos. Chem. Phys.* **2011**, *11*, 393–406. [[CrossRef](#)]
33. Tang, W.; Yang, K.; Qin, J.; Li, X.; Niu, X. A 16-year dataset (2000–2015) of high-resolution (3 h, 10 km) global surface solar radiation. *Earth Syst. Sci. Data* **2019**, *11*, 1905–1915. [[CrossRef](#)]
34. Hersbach, H.; Bell, B.; Berrisford, P.; Hirahara, S.; Horányi, A.; Muñoz-Sabater, J.; Nicolas, J.; Peubey, C.; Radu, R.; Schepers, D. The ERA5 global reanalysis. *Q. J. R. Meteorol. Soc.* **2020**, *146*, 1999–2049. [[CrossRef](#)]
35. Savtchenko, A.; Ouzounov, D.; Ahmad, S.; Acker, J.; Leptoukh, G.; Koziana, J.; Nickless, D. Terra and Aqua MODIS products available from NASA GES DAAC. *Adv. Space Res.* **2004**, *34*, 710–714. [[CrossRef](#)]
36. Práválie, R.; Patriche, C.; Bandoc, G. Spatial assessment of solar energy potential at global scale. A geographical approach. *J. Clean. Prod.* **2019**, *209*, 692–721. [[CrossRef](#)]
37. Günen, M.A. Determination of the suitable sites for constructing solar photovoltaic (PV) power plants in Kayseri, Turkey using GIS-based ranking and AHP methods. *Environ. Sci. Pollut. Res.* **2021**, *28*, 57232–57247. [[CrossRef](#)]
38. Wu, F.; Fu, C. Assessment of GEWEX/SRB version 3.0 monthly global radiation dataset over China. *Meteorol. Atmos. Phys.* **2011**, *112*, 155–166. [[CrossRef](#)]
39. Xia, X.A.; Wang, P.C.; Chen, H.B.; Liang, F. Analysis of downwelling surface solar radiation in China from National Centers for Environmental Prediction reanalysis, satellite estimates, and surface observations. *J. Geophys. Res. Atmos.* **2006**, *111*, D9. [[CrossRef](#)]
40. Yang, K.; Koike, T.; Stackhouse, P.; Mikovitz, C.; Cox, S.J. An assessment of satellite surface radiation products for highlands with Tibet instrumental data. *Geophys. Res. Lett.* **2006**, *33*, L22403. [[CrossRef](#)]
41. Yang, K.; Pinker, R.T.; Ma, Y.; Koike, T.; Wonsick, M.M.; Cox, S.J.; Zhang, Y.; Stackhouse, P. Evaluation of satellite estimates of downward shortwave radiation over the Tibetan Plateau. *J. Geophys. Res. Atmos.* **2008**, *113*, D17. [[CrossRef](#)]

42. Zhang, X.; Lv, N.; Yao, L.; Jiang, H. Error analysis of ECMWF surface solar radiation data in China. *J. Geo Inf. Sci.* **2018**, *20*, 254–267.
43. Ma, Q.; Wang, K.; Wild, M. Impact of geolocations of validation data on the evaluation of surface incident shortwave radiation from Earth System Models. *J. Geophys. Res. Atmos.* **2015**, *120*, 6825–6844. [[CrossRef](#)]
44. Huang, G.; Li, Z.; Li, X.; Liang, S.; Yang, K.; Wang, D.; Zhang, Y. Estimating surface solar irradiance from satellites: Past, present, and future perspectives. *Remote Sens. Environ.* **2019**, *233*, 111371. [[CrossRef](#)]
45. Zhang, J.; Shen, R.; Shi, C.; Bai, L.; Liu, J.; Sun, S. Evaluation and comparison of downward solar radiation from new generation atmospheric reanalysis ERA5 across mainland China. *J. Geo Inf. Sci.* **2021**, *23*, 2261–2274.
46. Pfeifroth, U.; Sanchez-Lorenzo, A.; Manara, V.; Trentmann, J.; Hollmann, R. Trends and Variability of Surface Solar Radiation in Europe Based On Surface- and Satellite-Based Data Records. *J. Geophys. Res. Atmos.* **2018**, *123*, 1735–1754. [[CrossRef](#)]
47. Sanchez-Lorenzo, A.; Enriquez-Alonso, A.; Wild, M.; Trentmann, J.; Vicente-Serrano, S.M.; Sanchez-Romero, A.; Posselt, R.; Hakuba, M.Z. Trends in downward surface solar radiation from satellites and ground observations over Europe during 1983–2010. *Remote Sens. Environ.* **2017**, *189*, 108–117. [[CrossRef](#)]
48. Li, B.; Yang, L.; Tang, S. Intraseasonal variations of summer convection over the Tibetan Plateau revealed by geostationary satellite FY-2E in 2010–2014. *J. Meteorol. Res.* **2019**, *33*, 478–490. [[CrossRef](#)]
49. Li, T.; Xin, X.; Zhang, H.; Yu, S.; Li, L.; Ye, Z.; Liu, Q.; Cai, H. Evaluation of Six Data Products of Surface Downward Shortwave Radiation in Tibetan Plateau Region. *Remote Sens.* **2024**, *16*, 791. [[CrossRef](#)]
50. Ren, L.; Lin, Z.; Yongjian, D. Variation characteristics of global radiation over the Tibetan Plateau during the past 40 years. *J. Glaciol. Geocryol.* **2012**, *34*, 1319–1327.
51. Kan, A.; Zeng, Y.; Meng, X.; Wang, D.; Xina, J.; Yang, X.; Tesren, L. The linkage between renewable energy potential and sustainable development: Understanding solar energy variability and photovoltaic power potential in Tibet, China. *Sustain. Energy Technol. Assess.* **2021**, *48*, 101551. [[CrossRef](#)]

**Disclaimer/Publisher’s Note:** The statements, opinions and data contained in all publications are solely those of the individual author(s) and contributor(s) and not of MDPI and/or the editor(s). MDPI and/or the editor(s) disclaim responsibility for any injury to people or property resulting from any ideas, methods, instructions or products referred to in the content.